nature communications

Article

https://doi.org/10.1038/s41467-025-67340-0

In-situ entropic ligand engineering enables high-efficiency quantum dot solar cells

Received: 21 July 2025

Accepted: 27 November 2025

Published online: 06 December 2025

Check for updates

Hehe Huang[1], Chenyu Zhao[1], Xuliang Zhang[1], Huifeng Li[1], Xinyu Zhao[1], Du Li[1], Chuanxiu Jiang[2,3], Lujie Jin[1], Xinfeng Liu[2,3], Youyong Li[1] & Jianyu Yuan[1]

Metal halide perovskite quantum dots (PQDs), particularly formamidinium lead triiodide ($FAPbI_3$) PQDs, have garnered significant attention for high-efficiency solar cells due to their ideal optical properties and stable phase structure. However, achieving desired colloidal dispersion and charge transport of $FAPbI_3$ PQDs still remains challenging. Herein, we report an efficient in-situ entropic ligand engineering strategy, using bis(2-ethylhexyl) phosphate (DEHP), to achieve improved dispersibility and charge transport in organic-inorganic hybrid $FAPbI_3$ PQDs. The branched 2-ethylhexyl tails of DEHP increase configurational entropy, improving solvent interaction and colloidal stability. In addition, the phosphinic acid head anchoring group of DEHP exhibits stronger binding strength for enhanced surface passivation and reduced core-core interactions. By optimizing the addition of entropic ligand, the DEHP-capped PQDs exhibit high colloidal stability and favorable optical properties, resulting in a power conversion efficiency (PCE) of 18.68% (certified value 18.23%) for PQD solar cells, along with improved stability. We believe these findings would provide insights to the design and synthesis of metal halide PQDs to construct desired films for optoelectronic applications.

The rise of lead halide thin-film perovskite has brought about an increasing interest in the corresponding nanostructured materials like quantum dots, nanoplates, nanowires[1–4]. Among them, three-dimensional confined perovskite quantum dots (PQDs) offering near perfect photoluminescent quantum yield, slow hot-carrier cooling time, high defect tolerance, especially their colloidal synthesis and processing using industrially friendly solvents[5–7], have been revolutionizing the sectors of light-emitting diodes[8], photovoltaic (PV)[9] and photodetectors[10]. Particularly in PQD based solar cells, the first report of inorganic $CsPbI_3$ PQDs reached an efficiency of 10.77% in 2016[11], and the highest reported efficiency boosted to a certified value of 18.1% for organic-inorganic hybrid $FAPbI_3$ (FA: formamidinium) PQDs in a very short period of time[12]. Given this increasing rate at device performances, PQD-integrated PV have attracted more attentions.

Currently, among all reported PQDs, the organic-inorganic hybrid $FAPbI_3$ is considered as the most promising candidate and recently dominate the research for high-efficiency and stable PQD PV due to its ideal optical bandgap, stable crystal, and phase structure[13–16]. Different from the bulk thin-film perovskites, PQD decouples crystallization from film deposition, therefore, the dispersibility and colloidal stability of PQD solutions are crucial for the quality of the active layer and PV performance of resultant PQD solar cells[17,18]. Unfortunately, the organic-inorganic hybrid $FAPbI_3$ PQDs are prone to aggregate due to the detachment of surface ligands and hydrogen bonding between organic cations during purification and storage process[19–21]. The dispersibility of PQD at solution state is primarily determined by the interactions between the organic ligand tail and the surrounding solvent. Therefore, the packing structure of the organic ligand tail is crucial for the colloidal stability[22]. Besides, unlike conventional metal chalcogenide quantum dots, $FAPbI_3$ PQDs with an organic-inorganic hybrid core exhibit greater complexity of core-core interactions. During the past few years, most efforts have been dedicated into the

[1]State Key Laboratory of Bioinspired Interfacial Materials Science, Institute of Functional Nano & Soft Materials (FUNSOM), Soochow University, Suzhou, PR China. [2]National Center for Nanoscience and Technology, Beijing, PR China. [3]University of Chinese Academy of Sciences, Beijing, PR China.
e-mail: jyyuan@suda.edu.cn

research of correlation between ligand head anchoring group and FA cations, with very few attentions to the tail groups and the structure of the ligand shell[23,24]. To further enhance the PV efficiency of $FAPbI_3$ PQD solar cells, it is important to achieve well-dispersed PQD solution for high-quality active layer fabrication. Inspired by the synthetic progress of conventional cadmium selenide quantum dots, the introduction of ligands with branched chains (entropy ligands) could restrict the packing of organic tails in solution, such an entropy ligand shell allows easier penetration of the surrounding solvent, therefore enhancing the dispersibility[25,26].

Along this line, we first reported the in-situ entropic ligand-anchoring for the synthesis of metal halide PQDs. To address the challenges in current hybrid PQDs, we introduced a branched entropy ligand, bis(2-ethylhexyl) phosphate (DEHP), into the hot-injection synthesis of $FAPbI_3$ PQDs. The two 2-ethylhexyl tail groups exhibit a branching and spreading nature. This structural characteristic would increase the spatial rotation of ligand tail at solution state to enhance interaction with the solvent and thereby enhancing the dispersibility. In addition, the head anchoring phosphinic acid group exhibits stronger binding strength to the surface relative to the native capping ligands oleic acid (OA) and oleate ammonium (OAm), thus suppressing core-core interactions at solution state. Through changing the mixing ratio of DEHP, the size of PQDs can be adjusted from ~13 to ~20 nm, and the optimal $FAPbI_3$ PQDs show greatly enhanced dispersibility and colloidal stability even at concentrated condition. To demonstrate the application of the entropic ligand engineered PQDs, we fabricated solar cells, delivering a best power conversion efficiency (PCE) of 18.68% with improved storage stability.

Results

Entropy ligand anchoring for PQD synthesis

As shown in Fig. 1a, the configurational entropy (S_{conf}, Supplementary Eq. 1) of different ligands was estimated according to their chain length and branching number. Linear ligands such as octanoic acid (OctOA) and OA exhibit relatively low configurational entropy due to limited conformational freedom. In contrast, the branched DEHP displays a much higher configurational entropy, attributed to its asymmetric side chains that increase the number of accessible conformations. This structural feature not only prevents dense ligand packing but also enhances colloidal stabilization and solvent penetration. Building upon these thermodynamic considerations, Fig. 1b illustrates the impact of different ligands on the dispersion and charge transport of $FAPbI_3$ PQDs. Long-chain OA ensures good colloidal stability in solution but severely limits charge transport due to large interparticle spacing. Short-chain OctOA reduces this spacing and thereby enhances charge transport[27], but its insufficient steric hindrance results in poor dispersion and aggregation. By contrast, DEHP provides a balanced solution: its strong phosphoric acid anchoring group secures surface passivation[28], while the branched alkyl tails introduce entropy-driven stabilization. Consequently, DEHP enables both good dispersion and efficient charge transport, effectively overcoming the limitations of conventional linear ligands.

To validate the entropy-driven design, we systematically replaced native OA/OAm with DEHP/OctOAm and examined morphological evolution. As shown in Fig. 1c, we first investigated the morphological properties of $FAPbI_3$ PQDs after replacing OA-OAm with DEHP-OctAm at molar ratios of 0%, 10%, 25%, 40%, 50%, 60%, 75%, and 100% using transmission electron microscopy (TEM), with the corresponding size distribution summarized in Supplementary Fig. 1a. When the replacement ratio ranges from 0% to 75%, the average size of the PQDs gradually increases from 14.03 nm to 19.18 nm. This effect may result from the combined influence of reduced steric hindrance[29], the acid-base equilibrium[30], and changes in nucleation and crystallization dynamics effected by DEHP, as revealed by the following in-situ characterizations. Further increasing the replacement ratio to 100%, the morphology and size of the PQDs is significantly changed. High angle annular dark field-scanning TEM (HAADF-STEM) elemental mapping in Supplementary Fig. 1b reveals the presence of phosphorus in these DEHP-capped $FAPbI_3$ PQDs. Supplementary Fig. 1c shows the ultraviolet-visible (UV-vis) and photoluminescence (PL) spectra of different $FAPbI_3$ PQD solutions. As the substitution ratio increases, the PL peak gradually redshifts, which is consistent with the observed increase in particle size from TEM measurements. For the PL quantum yields (PLQY) measurements, the 50% replacement ratio reaches a PLQY value of 98.4%, which is in line with the time resolved PL (TRPL) characterizations (Supplementary Fig. 2), suggesting that the 50% replacement ratio yields the optimal $FAPbI_3$ PQDs. All these results indicate that the both the steric hindrance of capping ligands and ligand-core/ligand-ligand interaction play a crucial role in controlling the size and morphology of the as-prepared PQDs in the hot-injection synthesis.

Growth kinetics and colloidal dispersity

To understand the impact of different ligand environments (OA, OctOA, and DEHP) on the PQD nucleation and growth processes, a set of characterizations were performed. In-situ PL, as depicted in Fig. 2a, is first employed to monitor the evolution of the synthesis of $FAPbI_3$ PQDs. Upon injecting FA-oleate into the PbI_2 precursor, the PL peak of $FAPbI_3$ PQDs appears immediately, indicating a rapid nucleation process. The PL intensity of OA-capped PQDs reaches its maximum within 10 s, while DEHP exhibits a slower process, with the PL intensity reaching its maximum at ~40 s (Fig. 2b). Such a difference indicates that DEHP-capped $FAPbI_3$ PQDs undergo a slower growth process relative to OA-capped PQDs. The delayed PL maximum in DEHP-capped PQDs suggests moderated growth kinetics, favoring monodispersion. In contrast, OctOA-capped $FAPbI_3$ PQDs exhibits a different trend. After the maximum, the PL intensity quickly decreases. This may be attributed to insufficient surface coverage of the $FAPbI_3$ PQDs, leading to aggregation of PQDs. After the same purification process, the absorption and PL spectra are shown in Fig. 2c. In comparison with DEHP, OctOA exhibits a more significant redshift relative to OA. The TEM analysis (Supplementary Fig. 3-4) reveals an average size of ~19 nm for OctOA-capped PQDs, which is similar with DEHP. Therefore, the further redshift of PL peak may be attributed to the PQD aggregation caused by the poorer dispersibility compared to DEHP-capped PQDs. X-ray diffraction (XRD) characterization shows that changes in the surface environment has negligible impact on the crystal structure, with all samples maintaining the cubic phase (Supplementary Fig. 5). The narrowing of the full-width at half maximum (FWHM) in the XRD peaks may be attributed to the increase in PQD size, which leads to reduced strain and improved crystallinity in the PQDs[31].

Dynamic light scattering (DLS) measurements were further conducted (Fig. 2d), where DEHP capped PQDs show a relatively narrow hydrodynamic size distribution, indicating better dispersion in solution, and the DEHP could effectively prevent aggregation. In contrast, OctOA-capped PQDs exhibit a broader size distribution with large hydrodynamic diameter, suggesting more aggregation and less uniform dispersion[18]. It is worth noting that, to maintain the acid–base equilibrium in the reaction system, a certain amount of OctOAm needs to be added after partial substitution of OA (Supplementary Fig. 6). In addition, to exclude any possible effect of OctOAm on the observed PQD properties, we conducted control experiments and characterized the resulting samples, as shown in the Supplementary Fig. 7. These results confirm that the improvements in dispersibility and device performance are specifically attributable to DEHP rather than the presence of OctOAm. To further study the colloidal stability of different $FAPbI_3$ PQDs, the change their PLQY value as a function of PQD concentration was measured and compared, with the results shown in Fig. 2e and Supplementary Fig. 8. After approximately 1000-fold dilution, the PLQY values of OA and OctOA capped $FAPbI_3$ PQDs

https://doi.org/10.1038/s41467-025-67340-0

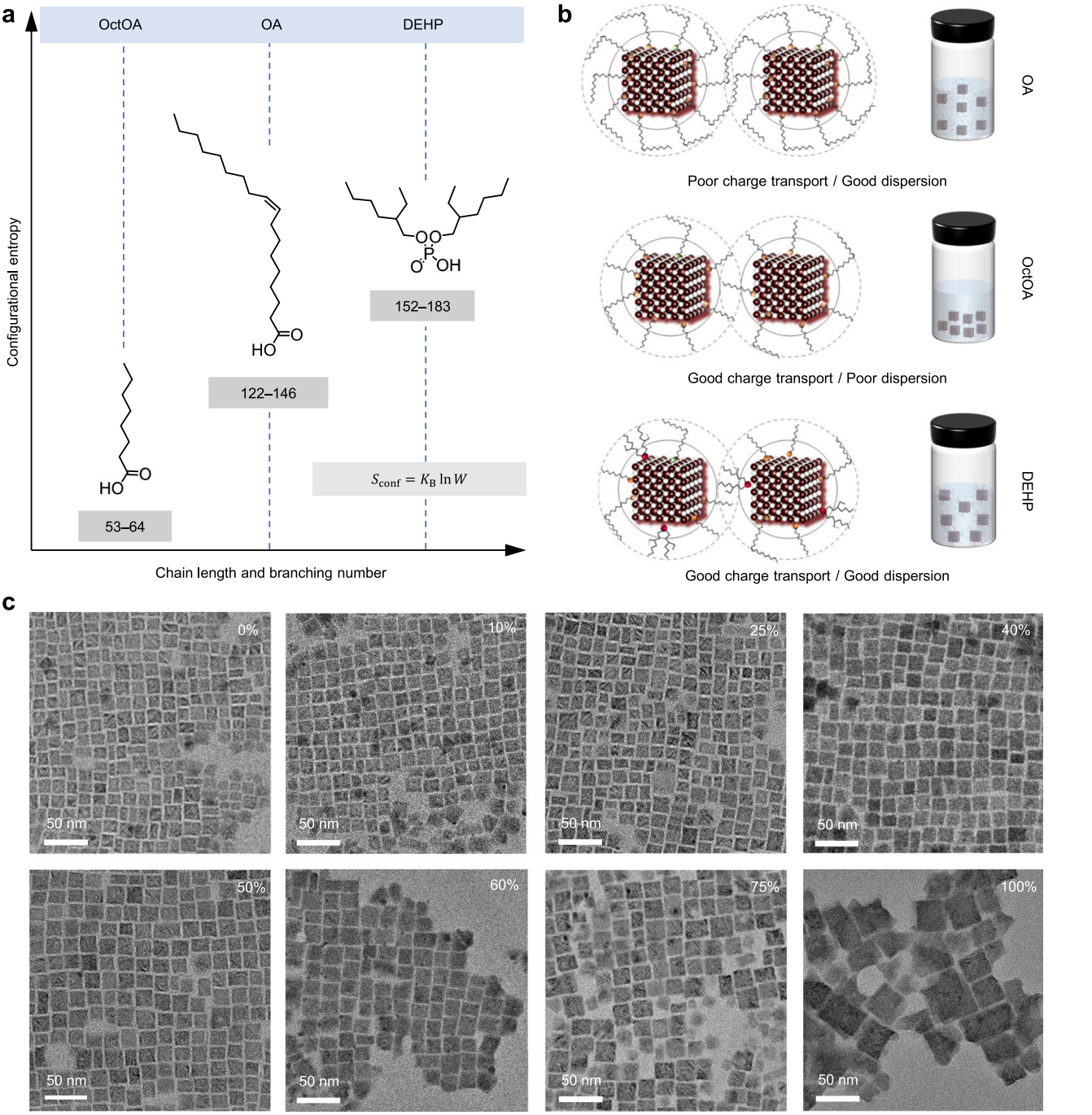

Fig. 1 | Entropy-driven ligand design. a The configuration entropy of different ligands (OctOA, OA, DEHP) as a function of chain length and branching number. The inserted equation, where S_{conf} is the configurational entropy per molecule ($J \cdot K^{-1}$), k_B is the Boltzmann constant, and W is the dimensionless number of accessible conformational microstates. **b** Schematic illustration of the ligand-dependent trade-off between charge transport and colloidal dispersion of PQDs. **c** The TEM images of $FAPbI_3$ PQDs that the native OA-OAm ligands partially replaced by DEHP-OctOAm from 0% to 100%.

display a significant decrease, whereas the DEHP-capped PQDs maintain a high PLQY value (over 85% of initial value). Similar results have been observed for the colloidal storage stability test, as shown in Fig. 2f, for a storage period of 90 days, the DEHP-capped PQD solution displays significantly improved colloidal stability. These results indicate that DEHP exhibits stronger adsorption energy, which could prevent ligand detachment from the PQD surface during the dilution process, therefore, suppress the formation of surface defects and non-radiative recombination, maintaining higher PLQY[32]. In order to further confirm the better surface passivation and solution stability, we also investigated the photostability of PQD solutions by monitoring their PL emission under continuous irradiation (405 nm). As presented in Fig. 2g and Supplementary Fig. 9, DEHP-capped PQD film exhibits a more significantly stable PL intensity compared to both OA and OctOA capped ones, retaining over 80% of their initial value after prolonged exposure. The enhanced photostability of DEHP-capped PQD films under 405 nm irradiation arises from the stronger binding of the phosphate group to Pb^{2+} surface sites and the higher configurational entropy of the branched ligand, which together suppress ligand desorption and mitigate photoinduced surface defects.

https://doi.org/10.1038/s41467-025-67340-0

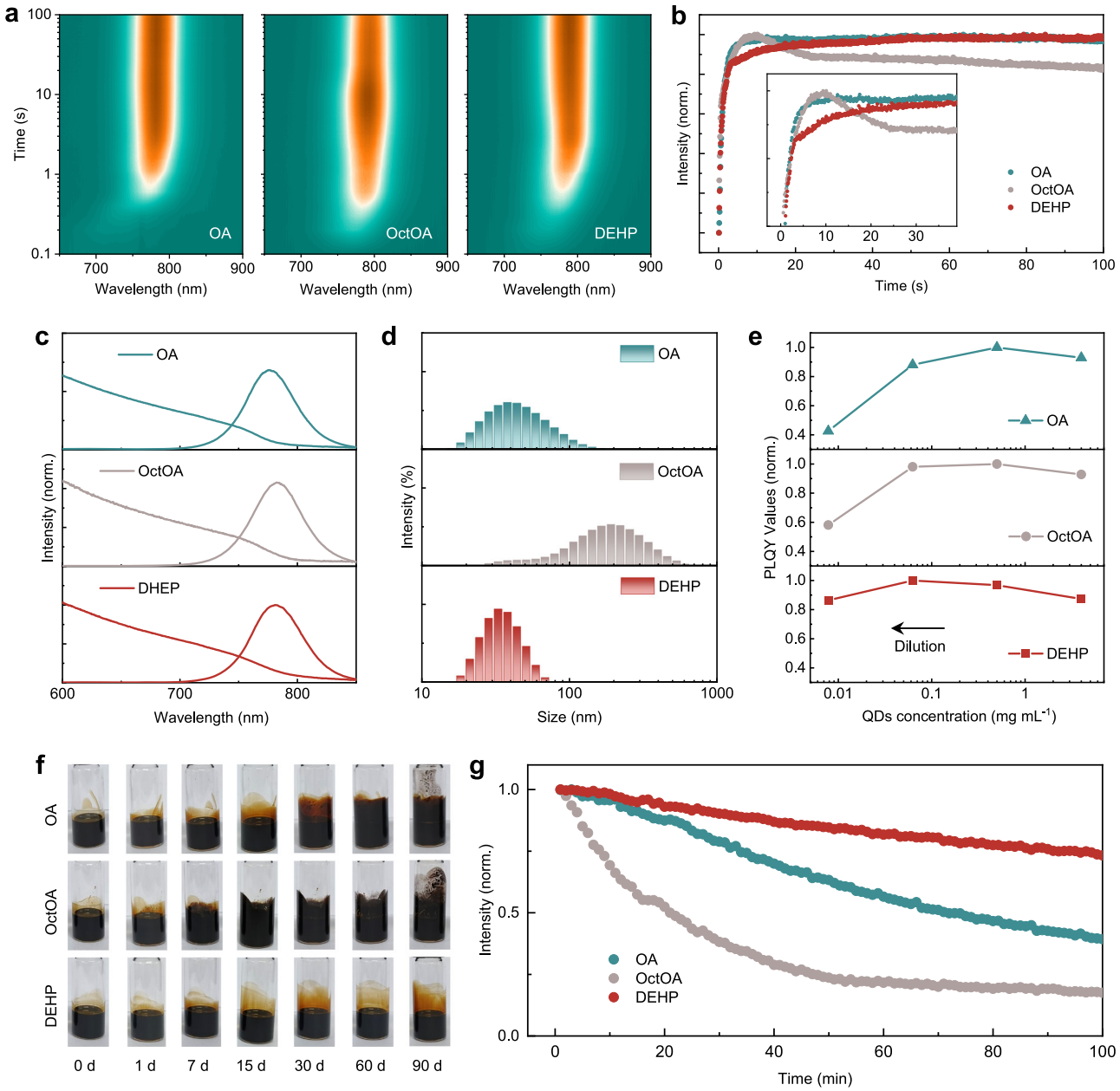

Fig. 2 | Dispersibility and stability of PQDs. a In-situ PL monitoring of the synthesis of OA, OctOA and DEHP-capped $FAPbI_3$ PQDs. **b** Time evolution curves of the PL intensity. **c** The absorption and PL spectra for the OA, OctOA and DEHP-capped PQD solution. **d** DLS spectra of $FAPbI_3$ PQD solutions in *n*-Hexane. **e** Normalized PLQY value as a function of the concentration for $FAPbI_3$ PQD solutions in *n*-Hexane. **f** Images of $FAPbI_3$ PQD solutions for storage stability test with the concentration of 80 mg/mL in n-octane under an air atmosphere. **g** The evolution of PL intensity of PQD solutions under continuous irradiation (405 nm, 0.1 W).

Surface chemistry of $FAPbI_3$ PQDs

Furthermore, more characterizations were performed to assess the change of surface chemistry. Figure 3a shows the electrostatic surface potential (ESP) of DEHP ligand. The molecular polarity of DEHP is slightly higher than that of OA, owing to the differences in their head groups: (-PO_4H) for DEHP and (-COOH) for OA (Supplementary Fig. 10). The change in polarity could affect the interaction between the ligand and $FAPbI_3$ PQD surface. To clarify the differences in interactions, we first performed Fourier-transform infrared (FTIR) spectroscopy characterization (Fig. 3b). Both samples exhibit a strong C=N stretching vibration at ~1710 cm^{-1}, which is attributed to the organic FA cation[19]. The intensity of the C-H stretching vibrations (2800–3000 cm^{-1}), primarily originating from the aliphatic chains of OA/OAm ligands, decreased from 69.8% to 56.6% (relative to the FA peak intensity) after DEHP capping of the PQDs. This is due to the replacement with short-chain DEHP ligands, which can enhance electronic coupling between adjacent PQDs[33]. To further elucidate the binding motif of DEHP, we performed ^{31}P nuclear magnetic resonance (NMR) analysis. As shown in Fig. 3c, the ^{31}P NMR spectrum indicates that the DEHP acts as an electron-donating ligand anchoring onto the $FAPbI_3$ PQD surface. Such an interaction further leads to a downfield shift in the ^{31}P NMR peak of the DEHP PQDs relative to the pristine DEHP molecules[14].

Then, we characterized both samples using X-ray photoelectron spectroscopy (XPS), as presented in the Fig. 3d–f and Supplementary Fig. 11. The appearance of the P 2*p* peak again confirms the adsorption of the DEHP ligand to the $FAPbI_3$ PQD surface. The Pb 4*f* and I 3*d* core-level spectral shift to lower binding energies for the DEHP-capped PQDs compared to the control OA-capped ones, suggesting that the

https://doi.org/10.1038/s41467-025-67340-0

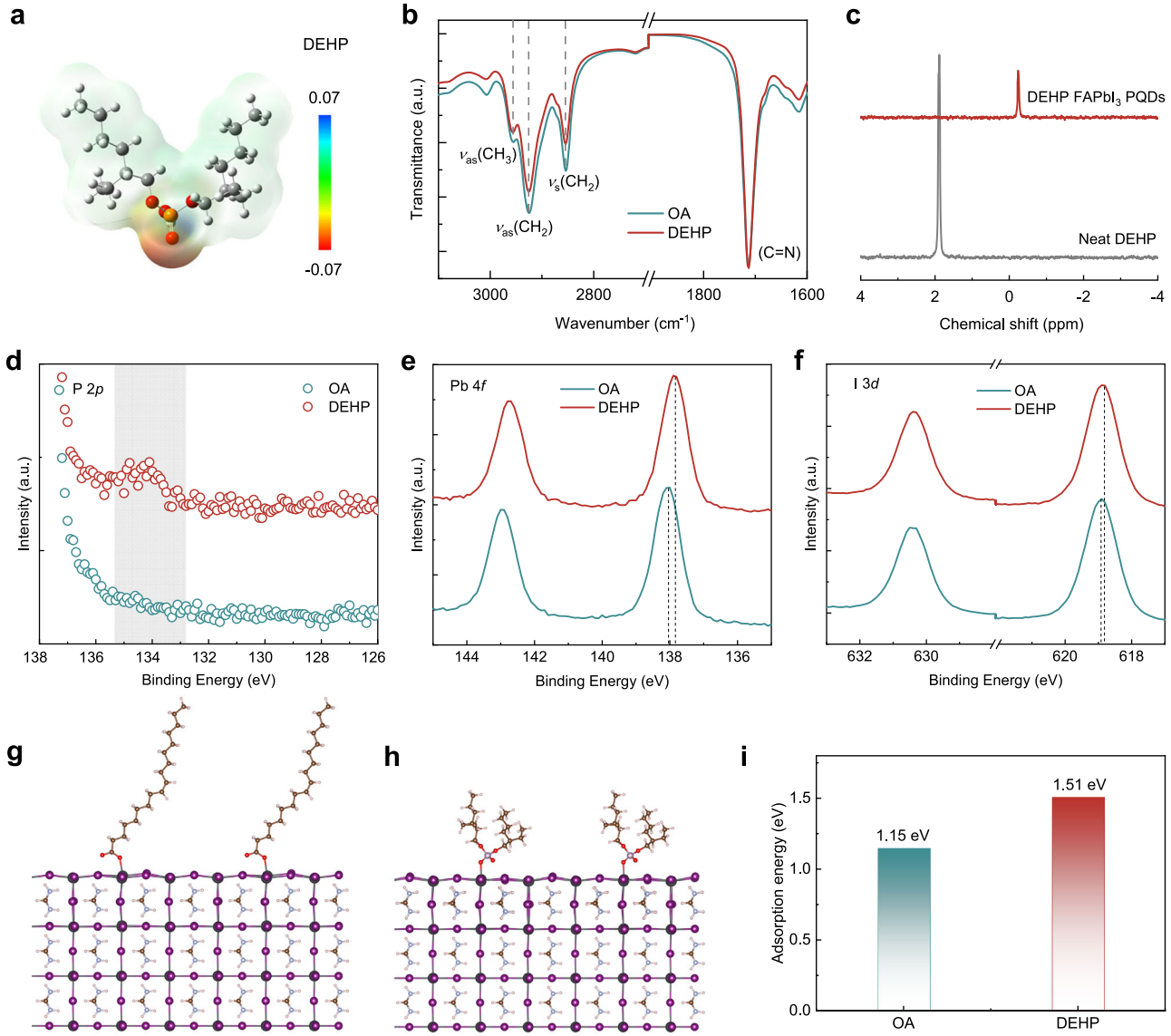

Fig. 3 | Surface chemical properties. a Electrostatic potential distribution in DEHP molecule. **b** FTIR spectra of OA and DEHP capped $FAPbI_3$ PQDs. **c** ^{31}P NMR spectra of as-synthesized DEHP PQDs and neat DEHP. XPS core-level spectra of (**d**) P *2p*, (**e**) Pb *4f*, and (**f**) I *3d*. DFT-simulated surface structure of (**g**) OA and (**h**) DEHP capped $FAPbI_3$ PQDs. **i** The calculated surface absorption free energy of OA and DEHP.

interaction between the DEHP ligand and the $FAPbI_3$ PQD surface leads to changes in the electronic environment of both Pb and I atoms. The electron-donating nature of DEHP would increase the electron density around these atoms, leading to a downfield shift in binding energy[34]. To further understand the bonding nature between the DEHP, OA ligands, and the QD surface, we then conducted density functional theory (DFT) calculations, with the results shown in Fig. 3g, h. The DFT results indicate that the DEHP ligand binds more strongly to the $FAPbI_3$ QD surface, primarily through the formation of a bond between the DEHP-P and $FAPbI_3$-Pb atoms. In specific, the calculated adsorption energy (E_{ad}) of DEHP is 1.51 eV, which is higher compared to OA (1.15 eV), confirming that DEHP exhibits a stronger binding affinity relative to the native OA ligand (Fig. 3i). The enhanced binding strength of DEHP to the $FAPbI_3$ surface could form a more robust interaction with the surface, reducing surface defects and promoting better charge transport[35].

Film morphology and charge transport

The solution and optical properties of PQDs significantly impact the morphology of the corresponding solid films, which is closely related to the performance of resultant solar cell devices. To evaluate the effect of the three different ligands on the solid-state film morphology, we first conducted scanning electron microscopy (SEM) characterization. As is shown in Fig. 4a, for OA- capped control $FAPbI_3$ PQDs, the film exhibits a relatively smooth surface with numerous pin-holes. This is primarily attributed to removal of the long-chain ligands during the post-treatment, which causes film shrinkage and the formation of voids due to the loss of surface coverage. In contract, the SEM image of OctOA-capped PQDs reveal the presence of large cracks and pores, indicating poor self-assembly and a tendency for aggregation (Fig. 4b). As expected, DEHP-capped PQDs with good colloidal dispersibility yield a smoother film with reduced surface cracks (Fig. 4c). The improved surface morphology may result from the fact that DEHP can prevent excessive aggregation of PQDs, and the ligand with short length could suppress volume shrinkage. Similar trend was also observed from the atomic force microscopy (AFM) (Supplementary Fig. 12) characterizations, further confirming that the DEHP-capped $FAPbI_3$ PQDs could deliver a smoother and denser PQD film. The DEHP-capped PQD film displays a uniform and narrow distribution of PL intensity; in contrast, the control OA-capped PQD film shows a lower

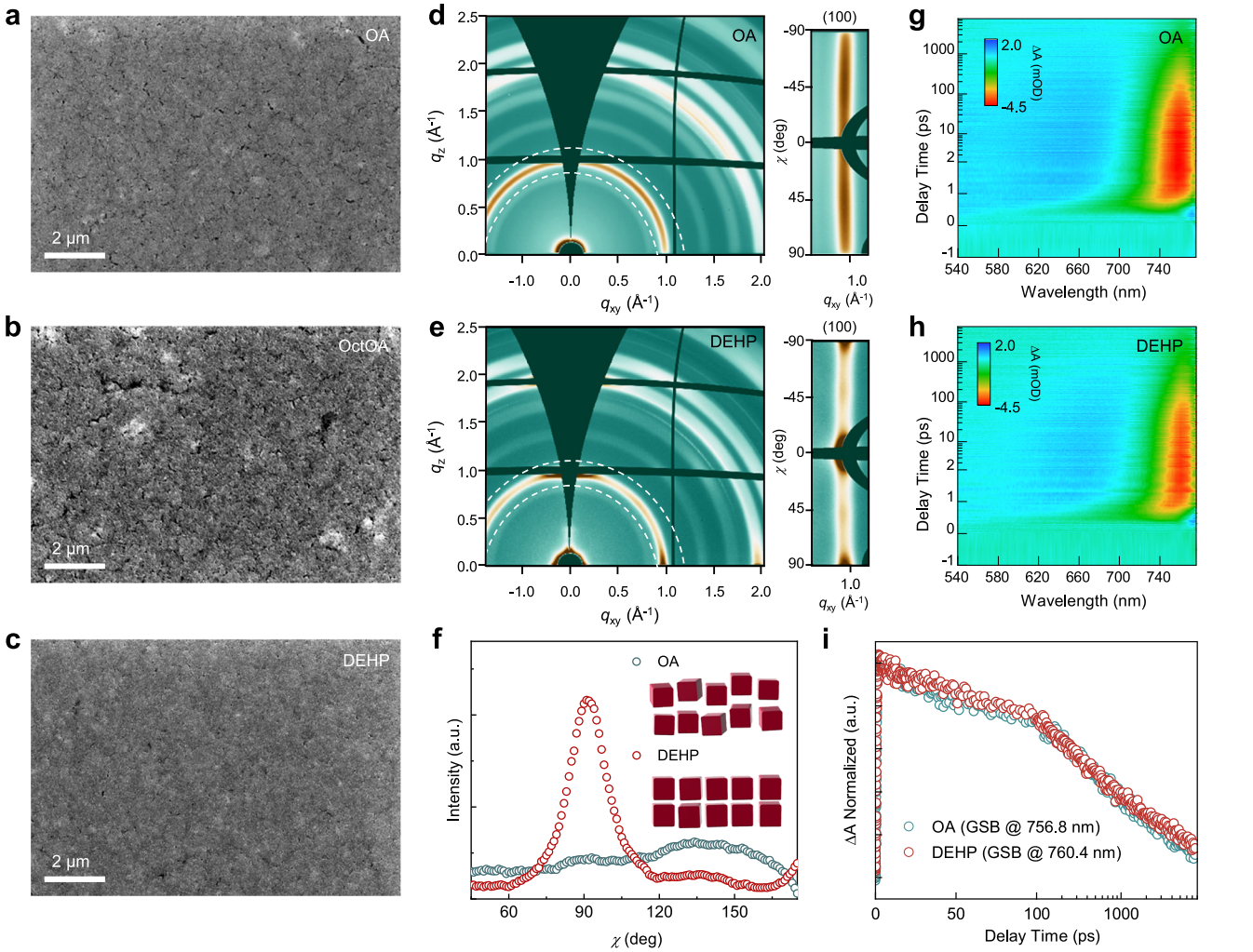

Fig. 4 | Film morphology and optoelectronic properties. a–c SEM images of $FAPbI_3$ PQD film with different surface ligand environment. 2D-GIWAXS patterns of (**d**) OA and (**e**) DEHP capped $FAPbI_3$ PQD films. **f** The corresponding (100) azimuthal integration of the (100) characteristic peak. Pseudocolour TA maps of (**g**) OA and (**h**) DEHP-capped $FAPbI_3$ PQD films. **i** The corresponding GSB decay spectra of OA and DEHP capped $FAPbI_3$ PQD films.

intensity (Supplementary Fig. 13). A homogeneous distribution of the PL intensity was beneficial for effective charge carrier extraction to suppress reduced nonradiative recombination[16].

Two-dimensional grazing incidence wide-angle X-ray scattering (2D-GIWAXS) was employed to investigate the crystal structure and stacking order of the $FAPbI_3$ PQD films. For the GIWAXS patterns shown in Fig. 4d-e, distinct diffraction rings corresponding (100), (110), (111), (200), and (210) planes are observed in both samples[13]. And the line-cut spectra extracted from the patterns (Supplementary Fig. 14) did not show apparent difference of peak position, indicating the same cubic crystal structures. In comparison, the DEHP-capped PQD film exhibits sharp and scattered Bragg peaks, besides, the sample displays stronger peak intensity in the radial integration intensity curve along the (100) direction at a 90° azimuthal angle (Fig. 4f). These observations indicate that the DEHP-capped PQDs exhibit improved ordering and stacking in the solid films, which is more favorable for charge transport along the vertical direction[9]. To gain more insight and an in-depth understanding of the charge carrier dynamics, we conducted femtosecond transient absorption (fs-TA) measurements, with the results shown in Fig. 4g, h and Supplementary Fig. 15. In the pseudo-color TA plot, a distinct negative signal corresponding to the ground-state bleaching (GSB) is observed at 756.8 nm for OA and 760.4 nm DEHP-capped PQDs, respectively. The carrier dynamics were extracted from the GSB decay data (Fig. 4i and Supplementary Table 1) using a triple exponential fitting model. The components τ_1, τ_2, and τ_3 correspond to the timescale of hot-phonon bottleneck, Auger recombination, and charge transport, respectively[14,36]. The overall lifetime of the DEHP PQD film is longer (τ_2: 664.0 ps, τ_3: 6964.8 ps) compared to that of OA (τ_2: 508.3 ps, τ_3: 6262.6 ps), indicating a lower trap-state density and more efficient carrier transport in the DEHP-coated PQDs.

High-efficiency $FAPbI_3$ PQD solar cells

Finally, $FAPbI_3$ PQD solar cells with a planar N-i-P device structure of glass/fluorine-doped tin oxide (FTO)/TiO_2 (40 nm)/$FAPbI_3$ PQD (~400 nm)/ poly[bis(4-phenyl)(2,4,6-trimethyl-phenyl)amine] (PTAA) (60 nm)/MoO_3 (8 nm)/Ag (120 nm) were fabricated. The cross-sectional SEM image in Fig. 5a clearly shows each corresponding layer of the device. The performance of the $FAPbI_3$ PQD solar cells was evaluated by measuring the current-voltage (J–V) characteristics under standard AM 1.5 G solar illumination at 100 mW cm^{-2}. Figure 5b presented the J–V curves of best-performing solar cells based on control OA and DEHP-capped $FAPbI_3$ PQDs, with corresponding device parameters listed Supplementary Table 2. For the OA-based control device, the optimal device shows a PCE of 15.92%, with a short-circuit current density (J_{SC}) of 19.83 mA cm^{-2}, an open-circuit voltage (V_{OC}) of 1.121 V, and a fill factor (FF) of 0.716. In contrast, the DEHP-based device exhibits a notable enhancement with a champion PCE of 18.68% (certified 18.23%; Supplementary Fig. 16). This is accompanied by an

https://doi.org/10.1038/s41467-025-67340-0

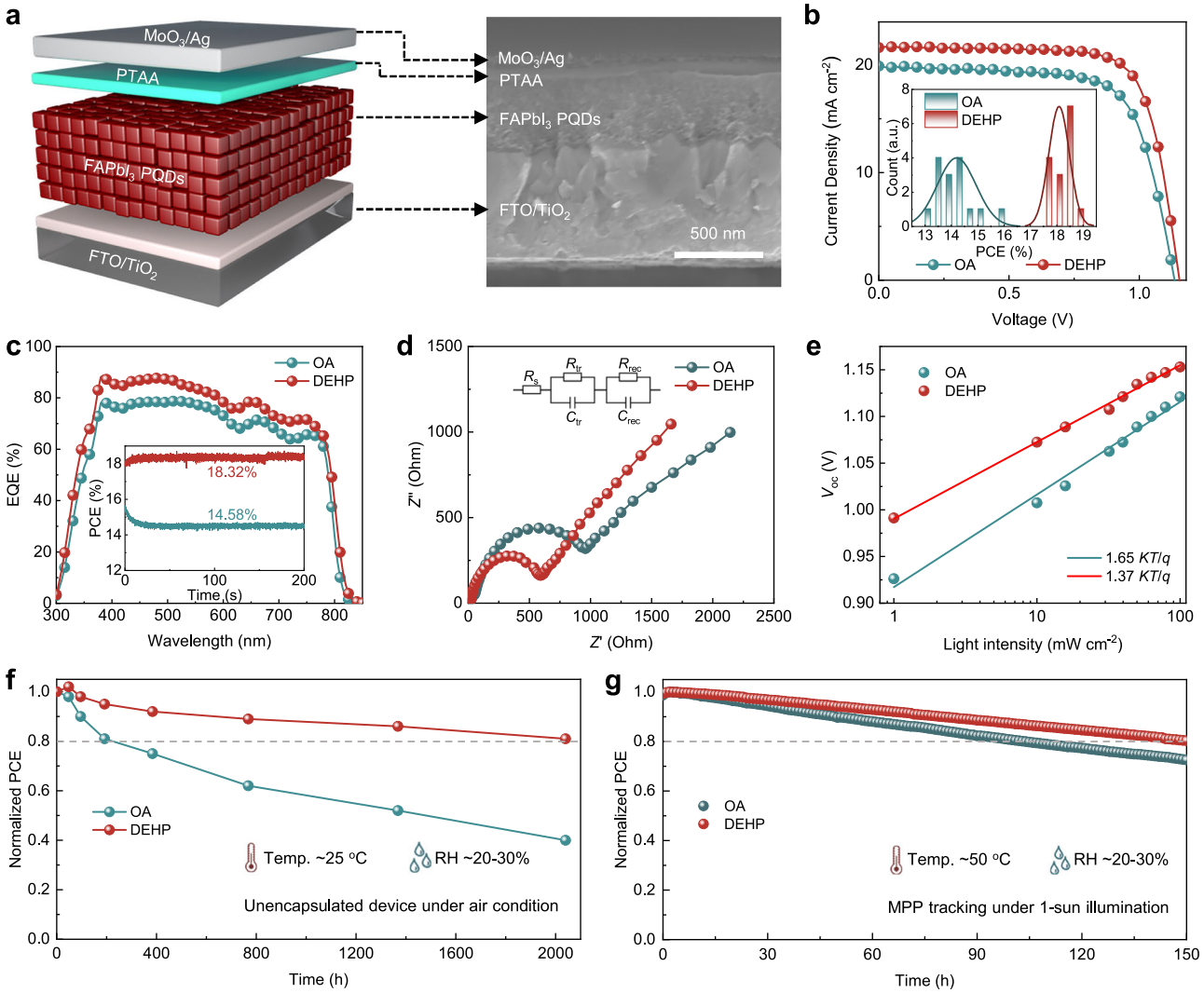

Fig. 5 | Device performance. a Schematic of N-i-P structure and corresponding cross-sectional SEM image of $FAPbI_3$ PQD solar cells. **b** *J-V* curves of best-performing OA and DEHP-capped $FAPbI_3$ PQD devices measured under the AM 1.5 G solar spectrum at 100 mW cm^{-2}, the inset shows the PCE distribution for 15 individual solar cells. **c** EQE and SPO curves of optimal OA and FDEHP -capped $FAPbI_3$ PQD devices. **d** Nyquist plots and **e** light intensity-dependent V_{OC} plots of OA- and DEHP-based $FAPbI_3$ PQD devices. **f** Long-term stability of unencapsulated $FAPbI_3$ PQD solar cells monitored under ambient conditions with a relative humidity between 20 and 30%. **g** MPP tracking of OA- and DEHP-based devices (unencapsulated) measured under 1-sun illumination (100 mW cm^{-2}) and ambient conditions (temperature of ~50 °C and relative humidity of 20–30%).

increased J_{SC} of 21.66 mA cm^{-2}, a V_{OC} of 1.153 V, and a FF of 0.748. It should be noted that this represents one of the highest certified efficiencies of PQD solar cells (Supplementary Table 3), highlighting the significance of entropic ligand mixing in the synthesis of high-quality hybrid PQDs with improved solution dispersibility and charge transport, ultimately leading to more efficient photovoltaic applications[13–15,37–39]. To assess the reproducibility of device performance, we evaluated the PCE distribution across 15 individual solar cells for each condition. The inset in Fig. 5b shows the histograms of the PCE values, where the DEHP-based devices consistently exhibit higher average efficiency and narrower distribution relative to OA-based control devices. For comparison, devices fabricated using OctOA-capped PQDs exhibit lower efficiency, reflecting the limited dispersibility and poor film quality of these PQDs (Supplementary Fig. 17). In addition, DEHP-based device shows negligible *J–V* hysteresis (Supplementary Fig. 18). All these device results indicate a more uniform and reliable performance in the DEHP-based PQD solar cells. Furthermore, to demonstrate the universality of this strategy, we further apply it to hybrid $MAPbI_3$ PQDs, which exhibits similar enhancements with better dispersibility and a highest reported PCE over 16% for $MAPbI_3$ PQD solar cells (Supplementary Fig. 19).

Meanwhile, J_{SC} integrated (Supplementary Fig. 20) from the external quantum efficiency (EQE) measurement well matches the values with the corresponding *J–V* curves, and the EQE of DEHP-based device (Fig. 5c) is enhanced in the whole photo-response region from 400 to 800 nm, suggesting better charge collection and reduced non-radiative recombination pathways, which is attributed to the enhanced surface passivation, electronic coupling and charge transport[40]. The inset of Fig. 5c shows the steady-state power output (SPO) at the maximum power point of both devices, where the DEHP devices also demonstrate a higher stable output, further confirming the reliability of enhanced performance. To elucidate the fundamental mechanisms underlying the enhanced photovoltaic performance of DEHP-based PQD solar cells, we further investigated their charge carrier dynamics. Electrochemical impedance spectroscopy reveals distinct differences between OA- and DEHP-based devices through Nyquist plots (Fig. 5d). The DEHP-based device exhibits significantly reduced charge transport resistance (R_{tr}) and enhanced recombination resistance (R_{rec}),

demonstrating improved charge transfer efficiency at the hetero-interfaces. Further analysis of V_{OC}-light intensity dependence (Fig. 5e) shows a decrease in the diode ideality factor from 1.65 (OA-based) to 1.37 (DEHP-based), indicating suppression of trap-assisted recombination. Moreover, the long-term stability was evaluated under different conditions. As shown in Fig. 5f, unencapsulated $FAPbI_3$ PQD solar cells were monitored under ambient conditions at a temperature of ~25 °C and a relative humidity of 20–30%. The DEHP-based device maintains over 81% of its initial efficiency after ageing for 2000 h, whereas that of the OA-based device retains ~40% of its original PCE. For the maximum power point tracking (Fig. 5g), unencapsulated devices were tested under continuous 1-sun illumination in ambient conditions (~50 °C, relative humidity 20–30%). The DEHP-based device exhibited a relatively lower PCE decay (20%) after 150 h, whereas the OA-based device showed a greater decay of approximately 28% over the same period. The long-term stability data indicate that DEHP-based devices exhibit significantly better retention of efficiency over time relative to OA-based devices. This suggests that the DEHP ligand enhances surface passivation and mitigate surface degradation, thereby contributing to more durable solar cell devices. In summary, these joint advancements of solution and optoelectronic properties demonstrate that DEHP ligand could prevent the aggregation of $FAPbI_3$ PQDs and assist their self-assembling through functional tail group, and the stronger anchoring head group effectively suppress the formation of defect states, promoting the DEHP-coated $FAPbI_3$ PQDs as ideal candidate for high-efficiency PQD solar cells.

Discussion

In summary, we reported an in-situ entropic ligand engineering strategy to synthesize high-quality and well-dispersed hybrid PQDs, addressing major challenges in current $FAPbI_3$ PQDs: colloidal dispersibility and charge transport. The 2-ethylhexyl tail groups exhibit a branching nature, further increasing the spatial rotation of ligand tail at solution state and thereby improving the dispersibility of the $FAPbI_3$ PQDs. The addition of entropic ligands not only mitigates non-radiative recombination but also promotes the dispersion of PQDs to achieve desired colloidal stability. Our results also demonstrate that the entropic ligand could form a robust ligand shell around PQD surfaces, which prevents degradation and maintains the cubic phase of $FAPbI_3$ over prolonged exposure. Finally, we have fabricated PQD solar cells, achieving a champion efficiency of 18.68% (certified value 18.23%), which is among the highest reported value to date. We believe these findings represent a critical advancement in the synthesis of high-quality organic-inorganic hybrid PQDs, which is essential for various optoelectronic applications.

Methods

Synthesis of $FAPbI_3$ PQDs

2.605 g of FAAc and 50 mL of OA were added to a 100 mL three-necked flask. The mixture was then subjected to vacuum stirring at 50 °C for 1 h to remove moisture and by-products. Subsequently, the flask was filled with N_2 and further heated to 120 °C, where it was maintained for 30 min. Finally, the resulting FA-OA was cooled to 70 °C and stored in an N_2-filled glovebox for the synthesis of $FAPbI_3$ PQDs. 0.344 g of PbI_2 and 20 mL of ODE were added to a 100 mL three-necked flask, followed by degassing at 90 °C for 30 min. Subsequently, different ratios of ligands were injected into the reaction mixture under a N_2 atmosphere, specifically: 4 mL of OA and 2 mL of OAm; 3.6 mL of OA, 1.8 mL of OAm, 0.2 mL of DEHP, and 0.1 mL of OctOAm; 3 mL of OA, 1.5 mL of OAm, 0.5 mL of DEHP, and 0.25 mL of OctOAm; 2.4 mL of OA, 1.2 mL of OAm, 0.8 mL of DEHP, and 0.4 mL of OctOAm; 2 mL of OA, 1 mL of OAm, 1 mL of DEHP, and 0.5 mL of OctOAm; 1.6 mL of OA, 0.8 mL of OAm, 1.2 mL of DEHP, and 0.6 mL of OctOAm; 1 mL of OA, 0.5 mL of OAm, 1.5 mL of DEHP, and 0.75 mL of OctOAm; 2 mL of DEHP and 1 mL of OctOAm, corresponding to replacement ratios of 0%, 10%, 25%, 40%, 50%, 60%, 75%, 100%, respectively. The mixture was degassed under vacuum until the reaction mixture became clear. Then, the temperature of the reaction mixture was lowered to 80 °C under a N_2 atmosphere, and 5 mL of the FA-OA solution was rapidly injected into the flask. After approximately 5–8 s, the reaction was quenched using an ice-water bath. After cooling to room temperature, the crude $FAPbI_3$ PQD solution was transferred into two centrifuge tubes. To each tube, 1 mL of toluene and 5 mL of MeOAc were added, and the mixture was centrifuged at 6780 × g (8000 rpm) for 30 min. Subsequently, the precipitate was redispersed in 7 mL of toluene, reprecipitated with 5 mL of MeOAc as an anti-solvent, and then centrifuged at 6780 × g (8000 rpm) for 10 min. The final precipitate was redispersed in 10 mL of n-hexane and stored at 4 °C for over 12 h for film deposition.

PQD Solar Cell Fabrication

A compact TiO_2 electron transporting layer of ~40 nm was deposited on cleaned glass/FTO substrate by chemical bath deposition at 70 °C, and then annealed at 200 °C for 30 min. Then, the $FAPbI_3$ PQD films were fabricated by layer-by-layer deposition. Each PQD layer was deposited using PQDs by spin coating at 1000 rpm for 15 s and 2000 rpm for 20 s. Then, 150 µL of FAI-IPA solution (3 mg mL^{-1}) was dropped onto the PQD solid for 5 s to remove the ligands, following by spinning at 2000 rpm for 20 s to remove the excess IPA and dry film. This process, operating in an air glove box with relative humidity of 15% and room temperature, was repeated three times to prepare a conductive PQD film for device fabrication. Subsequently, 15 mg mL^{-1} PTAA-toluene solution doped by LAD was spin coated on PQD film to deposit hole transporting layer. Finally, MoO_3 (8 nm) and Ag (120 nm) electrode was deposited by thermal evaporator. The active area of 0.0725 cm^2 was defined by a shadow mask, and an aperture mask of 0.04 cm^2 was used during the test of the 0.0725-cm^2-sized cells.

Reporting summary

Further information on research design is available in the Nature Portfolio Reporting Summary linked to this article.

Data availability

All data generated in this study are provided in the article and Supplementary Information and the raw data supporting this study are available from the Source Data file. Source data are provided with this paper.

References

1. Garcia de Arquer, F. P. et al. Semiconductor quantum dots: technological progress and future challenges. *Science* **373**, eaaz8541 (2021).
2. Xiao, S., Mei, X. & Zhang, X. Surface matrix regulation of perovskite quantum dots for efficient solar cells. *Energy Environ. Sci.* **17**, 5756–5794 (2024).
3. Bian, Y. et al. Efficient green InP-based QD-LED by controlling electron injection and leakage. *Nature* **635**, 854–859 (2024).
4. Li, H. et al. Buried interface engineering enables efficient and refurbished $CsPbI_3$ perovskite quantum dot solar cells. *Energy Environ. Sci.* **18**, 972–981 (2025).
5. Protesescu, L. et al. Nanocrystals of cesium lead halide perovskites ($CsPbX_3$, X = Cl, Br, and I): novel optoelectronic materials showing bright emission with wide color gamut. *Nano Lett.* **15**, 3692–3696 (2015).
6. Morad, V. et al. Designer phospholipid capping ligands for soft metal halide nanocrystals. *Nature* **626**, 542–548 (2024).
7. Akkerman, Q. A. et al. Controlling the nucleation and growth kinetics of lead halide perovskite quantum dots. *Science* **377**, 1406–1412 (2022).
8. Dong, Y. et al. Bipolar-shell resurfacing for blue LEDs based on strongly confined perovskite quantum dots. *Nat. Nanotechnol.* **15**, 668–674 (2020).

9. Jia, D., Chen, J., Zhuang, R., Hua, Y. & Zhang, X. Inhibiting lattice distortion of $CsPbI_3$ perovskite quantum dots for solar cells with efficiency over 16.6%. *Energy Environ. Sci.* **15**, 4201–4212 (2022).
10. Zhao, C. et al. Fast organic cation exchange in colloidal perovskite quantum dots toward functional optoelectronic applications. *J. Am. Chem. Soc.* **146**, 4913–4921 (2024).
11. Swarnkar, A. et al. Quantum dot-induced phase stabilization of α-$CsPbI_3$ perovskite for high-efficiency photovoltaics. *Science* **354**, 92–95 (2016).
12. Aqoma, H. et al. Alkyl ammonium iodide-based ligand exchange strategy for high-efficiency organic-cation perovskite quantum dot solar cells. *Nat. Energy* **9**, 324–332 (2024).
13. Zhang, X. et al. Ligand-assisted coupling manipulation for efficient and stable $FAPbI_3$ colloidal quantum dot solar cells. *Angew. Chem. Int. Ed.* **62**, e202214241 (2022).
14. Zhang, X. et al. Conductive colloidal perovskite quantum dot inks towards fast printing of solar cells. *Nat. Energy* **9**, 1378–1387 (2024).
15. Ding, S. et al. In situ bonding regulation of surface ligands for efficient and stable $FAPbI_3$ quantum dot solar cells. *Adv. Sci.* **9**, e2204476 (2022).
16. Jia, D. et al. Surface matrix curing of inorganic $CsPbI_3$ perovskite quantum dots for solar cells with efficiency over 16%. *Energy Environ. Sci.* **14**, 4599–4609 (2021).
17. Tseng, Z. L. et al. Aggregation control, surface passivation, and optimization of device structure toward near-infrared perovskite quantum-dot light-emitting diodes with an EQE up to 15.4%. *Adv. Mater.* **34**, e2109785 (2022).
18. Huang, H. et al. High-efficiency perovskite quantum dot photovoltaic with homogeneous structure and energy landscape. *Adv. Funct. Mater.* **33**, 2210728 (2023).
19. Xue, J. et al. Surface ligand management for stable $FAPbI_3$ perovskite quantum dot solar cells. *Joule* **2**, 1866–1878 (2018).
20. Hao, M. et al. Ligand-assisted cation-exchange engineering for high-efficiency colloidal $Cs_{1-x}FA_xPbI_3$ quantum dot solar cells with reduced phase segregation. *Nat. Energy* **5**, 79–88 (2020).
21. Wang, S. et al. Thermal tolerance of perovskite quantum dots dependent on A-site cation and surface ligand. *Nat. Commun.* **14**, 2216 (2023).
22. Calvin, J. J., Brewer, A. S. & Alivisatos, A. P. The role of organic ligand shell structures in colloidal nanocrystal synthesis. *Nat. Synth.* **1**, 127–137 (2022).
23. Zhang, M. et al. Renovating the surface matrix of $FAPbI_3$ perovskite quantum dots via phase-transfer catalysis for 16.29% efficiency solar cells. *Energy Environ. Sci.* **17**, 2145–2156 (2024).
24. Bai, Y., Hao, M., Ding, S., Chen, P. & Wang, L. Surface chemistry engineering of perovskite quantum dots: strategies, applications, and perspectives. *Adv. Mater.* **34**, 2105958 (2021).
25. Yang, Y., Qin, H. & Peng, X. Intramolecular entropy and size-dependent solution properties of nanocrystal-ligands complexes. *Nano Lett.* **16**, 2127–2132 (2016).
26. Yang, Y. et al. Entropic ligands for nanocrystals: from unexpected solution properties to outstanding processability. *Nano Lett.* **16**, 2133–2138 (2016).
27. Chen, K. et al. Short-Chain Ligand-Passivated Stable α-$CsPbI_3$ quantum dot for all-inorganic perovskite solar cells. *Adv. Funct. Mater.* **29**, 1900991 (2019).
28. Li, H. et al. Nanosurface-reconstructed perovskite for highly efficient and stable active-matrix light-emitting diode display. *Nat. Nanotechnol.* **19**, 638–645 (2024).
29. Pan, A. et al. Insight into the ligand-mediated synthesis of colloidal $CsPbBr_3$ perovskite nanocrystals: the role of organic acid, base, and cesium precursors. *ACS Nano* **10**, 7943–7954 (2016).
30. Almeida, G. et al. Role of acid–base equilibria in the size, shape, and phase control of cesium lead bromide nanocrystals. *ACS Nano* **12**, 1704–1711 (2018).
31. Huang, H. et al. Controllable colloidal synthesis of $MAPbI_3$ perovskite nanocrystals for dual-mode optoelectronic applications. *Nano Lett.* **23**, 9143–9150 (2023).
32. Zhang, B. et al. Alkyl phosphonic acids deliver $CsPbBr_3$ nanocrystals with high photoluminescence quantum yield and truncated octahedron shape. *Chem. Mater.* **31**, 9140–9147 (2019).
33. Anderson, N. C., Hendricks, M. P., Choi, J. J. & Owen, J. S. Ligand exchange and the stoichiometry of metal chalcogenide nanocrystals: spectroscopic observation of facile metal-carboxylate displacement and binding. *J. Am. Chem. Soc.* **135**, 18536–18548 (2013).
34. Li, C., Zhang, N. & Gao, P. Lessons learned: how to report XPS data incorrectly about lead-halide perovskites. *Mater. Chem. Front.* **7**, 3797–3802 (2023).
35. Pan, J. et al. Bidentate ligand-passivated $CsPbI_3$ perovskite nanocrystals for stable near-unity photoluminescence quantum yield and efficient red light-emitting diodes. *J. Am. Chem. Soc.* **140**, 562–565 (2018).
36. Ghasemi, M., Lu, J., Jia, B. & Wen, X. Steady state and transient absorption spectroscopy in metal halide perovskites. *Chem. Soc. Rev.* **54**, 1644–1683 (2025).
37. Zhao, C. et al. Fluorinated pseudo-halide anion enables >19% efficiency and durable perovskite quantum dot solar cells. *Adv. Mater.* **37**, e12201 (2025).
38. Jia, D. et al. Enriching conductive capping by alkaline treatment of perovskite quantum dots towards certified 18.3%-efficient solar cells. *Nat. Commun.* **16**, 8612 (2025).
39. Zhang, M. et al. Consecutive surface matrix engineering of $FAPbI_3$ perovskite quantum dots for solar cells with over 19% efficiency. *Energy Environ. Sci.* **18**, 8964–8976 (2025).
40. Wang, Y. et al. Surface ligand management aided by a secondary amine enables increased synthesis yield of CSPBi3 perovskite quantum dots and high photovoltaic performance. *Adv. Mater.* **32**, e2000449 (2020).

Acknowledgements

This work was financially supported by the National Key Research and Development Program of China (No. 2023YFE0210000) (J.Y), the National Natural Science Foundation of China (No. 52261145696 (J.Y), 52473187 (J.Y), and 22405186 (X.Z)), Natural Science Foundation of Jiangsu Province (BK20240763 (X.Z)), "111" project, Collaborative Innovation Center of Suzhou Nano Science and Technology, Soochow University.

Author contributions

J.Y. conceived and supervised the project. H.H. conducted the PQD synthesis and most of characterizations and experimental analysis. C.Z., X.Z. (Zhang), H.L., X.Z. (Zhao) and the D.L. fabricated the PQD devices and device characterizations. C.J. and X.L. conducted the carrier dynamic characterizations. L.J. and Y.L. performed simulated characterizations. H.H. drafted the manuscript, and J.Y. revised manuscript with contributions from all authors.

Competing interests

The authors declare no competing interests.

Additional information

Supplementary information The online version contains supplementary material available at https://doi.org/10.1038/s41467-025-67340-0.

Correspondence and requests for materials should be addressed to Jianyu Yuan.

Peer review information *Nature Communications* thanks the anonymous, reviewer(s) for their contribution to the peer review of this work. A peer review file is available.